Ocean Modelling xxx (2014) xxx–xxx

Contents lists available at ScienceDirect

Ocean Modelling

journal homepage: www.elsevier.com/locate/ocemod

Lagrangian reconstructions of temperature and velocity in a model of surface ocean turbulence

Stefano Berti [a,b,*], Guillaume Lapeyre [b]

[a] Laboratoire de Mécanique de Lille, CNRS/UMR 8107, Université Lille 1, 59650 Villeneuve d'Ascq, France
[b] Laboratoire de Météorologie Dynamique, IPSL, CNRS/ENS, Paris, France

ARTICLE INFO

Article history:
Received 19 September 2013
Received in revised form 10 February 2014
Accepted 18 February 2014
Available online xxxx

Keywords:
Lagrangian transport
Surface temperature
Oceanic turbulence
Submesoscales

ABSTRACT

The characterization of submesoscale dynamics is crucial to apprehend their impact on the global ocean properties. Direct measurements of fine structures over the world oceans, nevertheless, are at present severely limited by the spatial resolution of available satellite products. In this work we numerically investigate the possibility to reconstruct tracer fields, like surface temperature, at small scales, from low-resolution data using a Lagrangian technique based on the properties of chaotic advection. The capabilities of the method are explored in the context of a forced Surface Quasi Geostrophic (SQG) turbulent flow representing a large-scale meandering jet and smaller-scale eddies. Both qualitative and quantitative comparisons are performed between the original (high-resolution) fields and their reconstructions that use only low-resolution data. Good agreement is found for filamentary structures, even in the presence of a large-scale forcing on the tracer dynamics. The statistics of tracer gradients, which are relevant for assessing the possibility to detect fronts, are found to be accurately reproduced. Exploiting SQG theory, the reconstruction technique is also extended to obtain the velocity field in three dimensions when temperature is the tracer. The results indicate that relevant features of dynamical quantities at small scales may be adequately deduced from only low-resolution temperature data. However, the ability to reconstruct the flow is critically limited by the energetic level of submesoscales. Indeed, only structures generated by non-local mesoscale features can be well retrieved, while those associated to the local dynamics of submesoscale eddies cannot be recovered.

1. Introduction

In recent years our picture of ocean dynamics has considerably evolved towards that of a highly complex system characterized by strong nonlinear interactions, whose spatiotemporal variability extends over a wide range of scales. In particular, the role played by relatively small scales is being viewed as more and more important. These scales, termed submesoscales, are characterized by thin ($\sim$10 km) filamentary and frontal structures elongated over several hundreds of kilometers (Ledwell et al., 1993), which are created by the stirring of mesoscale ($\sim$100 km) eddies. Here we define submesoscales in a broad sense, as scales below the deformation radius, with relative vorticities of the order of the Coriolis frequency. This generally implies order one Rossby number and ageostrophic velocities comparable in magnitude to the geostrophic ones (but note, too, that QG theory has been shown to still apply at these scales, see e.g., Klein et al., 2008). Signatures of such features have been detected in high-resolution observations of sea surface temperature (SST) and ocean color. Recent theoretical work suggests that submesoscale fronts play a leading role in the vertical transport of biochemical tracers and heat exchanges (Lévy, 2008; Klein and Lapeyre, 2009; Ferrari, 2011). Indeed, high-resolution three-dimensional (3D) numerical simulations showed that the energetic content of submesoscales is much higher than previously hypothesized (Capet et al., 2008; Klein et al., 2008).

A major problem in studying submesoscale dynamics, however, is that we still practically have no experimental access to these scales, except for in situ observations (Thomas et al., 2010; Shcherbina et al., 2010; Cole and Rudnick, 2012) or for data from surface drifters (see, e.g., LaCasce and Ohlmann, 2003; Koszalka et al., 2009; Lumpkin and Elipot, 2010; Berti et al., 2011). On a global scale, direct measurement of submesoscale features is limited by the spatial resolution of available satellite products. For instance, altimetry now routinely provides measurements over the world oceans of surface currents, geostrophically derived from sea surface height (SSH), but it only allows to resolve structures of size

* Corresponding author. Address: Polytech'Lille, avenue Paul Langevin, 59650 Villeneuve d'Ascq, France. Tel.: +33 328767394.
E-mail address: stefano.berti@polytech-lille.fr (S. Berti).

http://dx.doi.org/10.1016/j.ocemod.2014.02.003
1463-5003/© 2014 Published by Elsevier Ltd.

~100 km (Le Traon et al., 1998). The resolution of the velocity fields can be enhanced through the use of combined altimeters (see, e.g., Pascual et al., 2006), but the requirements needed for resolving submesoscale motions are still not met. Similarly, estimates of SST from microwave radiometers, such as AMSR-E, have a resolution of order 50 km, also not suited for the direct detection of submesoscale structures. High-resolution products are also available, such as those obtained from instruments like AVHRR which provide SST data at a resolution of about 1 km. Nevertheless, even in this case it is rare to have good quality images over large regions, due to cloud coverage.

Together with the efforts dedicated to improving the knowledge of horizontal surface flows, a further great challenge for the oceanographic community is currently represented by the determination of the full 3D structure of submesoscale features. While satellites provide information on the ocean surface, subsurface information is considerably more difficult to retrieve.

In order to tackle the above questions an interesting approach is to resort to new techniques, relying on transport processes, that suggest the possibility to infer some characteristics of submesoscale dynamics from low-resolution data (SSH or SST). In this paper we consider a Lagrangian method, based on the properties of chaotic advection (Ottino, 1989) or the tracer cascade to small scales (Batchelor, 1959), for the reconstruction of small scales and fronts of SST. Our main goal here is to test such a method in numerical simulations of upper-ocean turbulence. The dynamical configuration we consider is obtained in the framework of the Surface Quasi Geostrophic (SQG) model (see e.g., Lapeyre and Klein, 2006), which has been shown to resemble surface flows like the Gulf Stream or the Antarctic Circumpolar Current, at mesoscale and submesoscale. In particular we will be concerned with the reconstruction of filamentary and frontal structures. Then, by exploiting the basic relations defining SQG dynamics, in conjunction with the Lagrangian technique, we provide an extension of the reconstruction method to calculate the 3D velocity field.

The paper is organized as follows. The first two sections are devoted to general aspects: in Section 2 we introduce the Lagrangian method of reconstruction, and in Section 3 we describe the flow configuration that is used, corresponding to an instance of forced SQG turbulence, that will create our synthetic SST high-resolution field. The analysis of the results obtained from reconstructions is presented in Section 4. There, we discuss the effect of reconstructions on SST fields by means of qualitative comparisons and we focus our attention on the quantification of statistical properties of reconstructed SST fields. In particular, we address the potential of the Lagrangian technique for the detection of fronts. We then consider the possibility to reconstruct the velocity field. In Section 5 we discuss how the dynamical properties of the advecting flow affect the quality of reconstructions. In particular we show that local dynamics of the velocity field represent a major limitation of the present method. Indeed, we find that only structures generated by the stirring of non-local mesoscale features can be well reconstructed, while oceanic submesoscales are often characterized by local dynamics. Finally, we offer a discussion and some conclusions in Section 6.

2. Lagrangian reconstruction method

Let $C(\mathbf{x},t)$ be a tracer field and $\mathbf{u}(\mathbf{x},t)$ the velocity field transporting it. The evolution of C is, then, described by the following equation:

$$\frac{\partial C}{\partial t} + \mathbf{u}\cdot\nabla C = H, \tag{1}$$

where H accounts for source and sink terms. If we assume that, at least in a certain range of scales, the contributions from sources and sinks are negligible, then the tracer is conserved along the Lagrangian flow:

$$\frac{DC}{Dt} = 0, \tag{2}$$

$$\frac{d\mathbf{x}(t)}{dt} = \mathbf{u}(\mathbf{x}(t),t). \tag{3}$$

This conservation property is at the base of the reconstruction technique we want to use.

The method of reconstruction of the tracer field consists in advecting a large number N_p of particles (defined by their position $\mathbf{x}_p$ and their tracer value $C(\mathbf{x}_p(t),t)$) with the flow field $\mathbf{u}$, i.e.,

$$\frac{d}{dt}\mathbf{x}_p = \mathbf{u}(\mathbf{x}_p,t), \tag{4}$$

where $p = 1,2,\ldots,N_p$ is an index labeling the trajectory associated with a particle. Under the hypothesis that the tracer is a passive field, by conservation of particle identity (Bennett, 2006), its value at the position (at time t) $\mathbf{x}_p(t)$ of a trajectory will be the same as the one at its Lagrangian origin ($\mathbf{x}_p(t-\tau_a)$ at the previous time $t-\tau_a$), i.e., $C(\mathbf{x}_p(t),t) = C(\mathbf{x}_p(t-\tau_a),t-\tau_a)$, and the latter can be assigned to the new particle position (see Fig. 1).

For low-resolution tracer fields, the property of chaotic advection to generate small-scale structures (Welander, 1955; Batchelor, 1959; Ottino, 1989) implies that the resulting tracer field computed at the new particle positions, i.e., the reconstructed one, will have a higher resolution than the low-resolution tracer field we start with. The method described above does not generally provide a tracer field on a regular grid: particles advected forward in time starting from uniformly spaced positions get concentrated in particular regions of space (e.g., eddies). However, one can easily avoid this inconvenient by advecting particles backward in time. Assume that we have a low-resolution tracer field at time $t-\tau_a$ on a regular grid of spacing Δx. The initial positions of the particles are chosen on the finer grid corresponding to the resolution we want to sample (at time t), with grid spacing $\delta x < \Delta x$. After advecting backward our particles, we assign to each particle the value of C at time $t-\tau_a$ by doing spatial interpolation on the low-resolution grid at time $t-\tau_a$ (see Fig. 1).

This method has been developed and validated for stratospheric flows (Sutton et al., 1994; Mariotti et al., 1997; Orsolini et al., 2001) and tropospheric flows (Legras et al., 2005). Concerning oceanic flows, it was recently used by Després et al. (2011a,b) to address the dynamics of frontal structures in the North Atlantic subpolar gyre, by advecting sea surface salinity (SSS) or SST with altimetry derived geostrophic flows. A critical review of Lagrangian methods using virtual tracers for diagnosing lateral mixing in the ocean has been recently carried out by Keating et al. (2011).

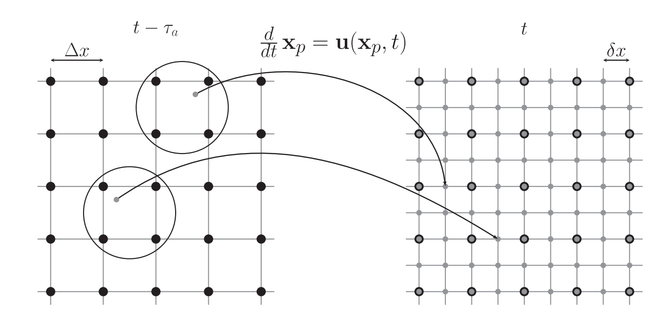

Fig. 1. Schematic view of the Lagrangian method (see text in Section 2) based on backward advection of synthetic particles from time t to time $t-\tau_a$.

3. Flow configuration and SQG turbulence

To apply the method described in Section 2, we are interested in working with a turbulent flow field characterized by the simultaneous presence of a jet and vortices, as the ones encountered in the real ocean (as, e.g., the Gulf Stream). In order to obtain such a flow, we consider the dynamics of surface temperature in the surface quasi-geostrophic approximation. This model has been proven to correctly represent mesoscale and submesoscale dynamics of the upper ocean layers (LaCasce and Mahadevan, 2006; Lapeyre and Klein, 2006; Isern-Fontanet et al., 2006, 2008), at least when SST is a good proxy of the density at mesoscale. Such a condition is expected to be met in the presence of a homogenized mixed-layer as, e.g., after strong wind events. Moreover, this type of dynamics can provide energetic submesoscales with spectral behavior close to the one found in high-resolution numerical integration of 3D primitive equations for a baroclinically unstable oceanic flow (Klein et al., 2008). Therefore, despite its idealized character, we expect the SQG model to carry some generality for oceanic flows. Note that more sophisticated models incorporating both classical QG vertical modes and the SQG solution exist (Tulloch and Smith, 2009; Wang et al., 2013).

In this framework the active tracer is sea surface temperature which evolves following

$$\partial_t \theta + \mathbf{u} \cdot \nabla \theta + \beta v = F + D. \tag{5}$$

The resulting dynamics is equivalent to that of a quasi-geostrophic flow with uniform potential vorticity (PV) (Held et al., 1995). Here θ is an anomaly of the whole SST field

$$\Theta \equiv \theta + \beta y \tag{6}$$

and β is a constant parameter that represents a mean temperature gradient ($\beta < 0$ in the northern hemisphere). The horizontal velocity $\mathbf{u} = (u, v)$ can be expressed in terms of a streamfunction ψ such that $(u, v) = (-\partial_y \psi, \partial_x \psi)$. The streamfunction is obtained from the surface temperature by inverting the uniform PV equation $\partial_x^2 \psi + \partial_y^2 \psi + \partial_z^2 \psi = 0$ subject to the boundary conditions: $\theta(z = 0) = \partial_z \psi|_{z=0}$ and $\psi \to 0$ for $z \to -\infty$, z being the vertical coordinate. Solving this system in Fourier space provides the relationship $\mathcal{F}(\psi) = \frac{\mathcal{F}(\theta)}{k}$ between temperature and velocity, where $\mathcal{F}()$ stands for the horizontal Fourier transform and k is the modulus of the horizontal wavenumber. Note that here we work with non-dimensional variables and we assume that density anomalies are proportional to the opposite of temperature anomalies.

The system is forced by a relaxation term

$$F = -\kappa(\langle \theta \rangle_x - \bar{\theta}), \tag{7}$$

where $\langle \cdots \rangle_x$ denotes a zonal average and $\bar{\theta}(y)$ is an assigned meridional temperature profile. This can be thought as a heat forcing from the atmosphere.

Eq. (5) is numerically integrated by means of a pseudo-spectral method in a square of size $L_0 = 2\pi$ with doubly periodic boundary conditions. The spatial resolution corresponds to $N_{hr} = 512$ grid points per direction and a 4th order Runge–Kutta scheme is used in time. With a doubly periodic model, it is generally not possible to confine a meandering jet, as the one we want to simulate, in the central part of the domain. Also, eddies tend to move in all directions, so that they can reenter the computational box from the north–south direction. To overcome this issue, a possible solution is to strongly damp perturbations at the northern and southern boundaries through a dissipative term D. That way, both the jet and the eddies will be localized in the central part of the domain, as it will be observed below. The dissipation D is parameterized by linear friction as $-f_d(y)\theta(x, y, t)/\tau$, with $f_d(y) = 1$ in two thin layers close to the boundaries and $f_d(y) = 0$ elsewhere. The dissipation coefficient is set to $1/\tau = 10.5$. Small-scale dissipation is taken into account by means of an exponential filter acting beyond a cut-off wavenumber $k_c = 40$ (LaCasce, 1996, 1998; Smith et al., 2001). For comparison purposes, in Section 5 we will also consider a flow with similar large-scale structures but less intense small scales, obtained by setting the cut-off wavenumber for small-scale dissipation to $k_c = 1$. This way, limitations of the reconstruction method related to the local or non-local dynamics of the advecting velocity field will be discussed.

The mean meridional temperature gradient is set to $\beta = -1.2$. Concerning the forcing, we choose a temperature profile which is nonzero only in two thin layers, where it has opposite sign, centered around $y_1 = L_0(1 - \delta)/2 \simeq 2$ and $y_2 = L_0(1 + \delta)/2 \simeq 4$ and smoothly matched by hyperbolic tangent functions. Specifically, we use the following expression:

$$\begin{aligned}\bar{\theta}(y) = A\Big\{ &\Big[1 - \tanh\Big(\frac{y - y_d}{\xi}\Big)\Big]\Big[1 + \tanh\Big(\frac{y - y_c}{\xi}\Big)\Big] \\ &- \Big[1 - \tanh\Big(\frac{y - y_b}{\xi}\Big)\Big]\Big[1 + \tanh\Big(\frac{y - y_a}{\xi}\Big)\Big]\Big\},\end{aligned} \tag{8}$$

where $A = 0.5, \xi = 1/8, y_{a,b} = L_0/2(1 - \delta \mp \epsilon), y_{c,d} = L_0/2(1 + \delta \mp \epsilon)$, with $\delta = 1/4$ and $\epsilon = 1/24$.

Moreover, we use the value $\kappa = 0.3$ for the relaxation rate appearing in Eq. (7). The configuration obtained from Eq. (8) is a generalization of the unstable temperature filament case studied in Held et al. (1995) and Juckes (1995) and is characterized by two temperature strips, each one unstable, creating a westerly jet between them.

Starting from random initial perturbations, after a transient period ($t < 70$) a statistically steady state is attained, as diagnosed from the temporal behavior of spatially averaged quantities, such as kinetic energy or enstrophy (not shown). In the following we will mainly refer to this regime; typically reconstructions will be considered in the interval $t \in [100, 150]$ and the origin of times will be shifted to $t_* = 100$.

The meridional profile of the zonal component of velocity $u(\mathbf{x}, t)$, zonally and temporally averaged, is shown in Fig. 2. An intense eastward jet can be noticed in the center of the domain, which is flanked by two weaker westward jets. In Fig. 3a we show a typical snapshot at a fixed time of the SST field Θ. The main characteristics are here easily recognized: a large-scale temperature gradient, a central meandering jet and several structures of different sizes, from large (mesoscale) eddies to small (submesoscale) filaments and vortices.

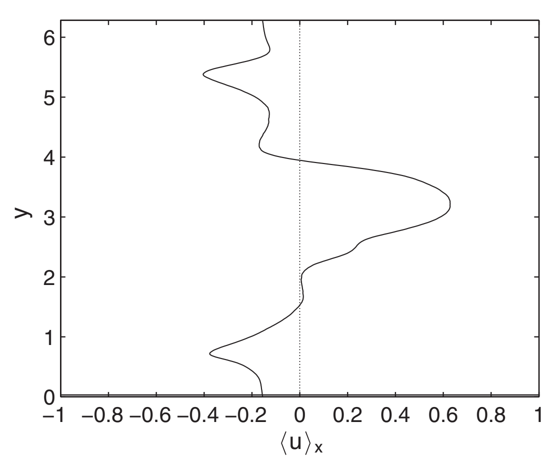

Fig. 2. Meridional profile of the zonal component of velocity averaged in time and in space along the zonal direction.

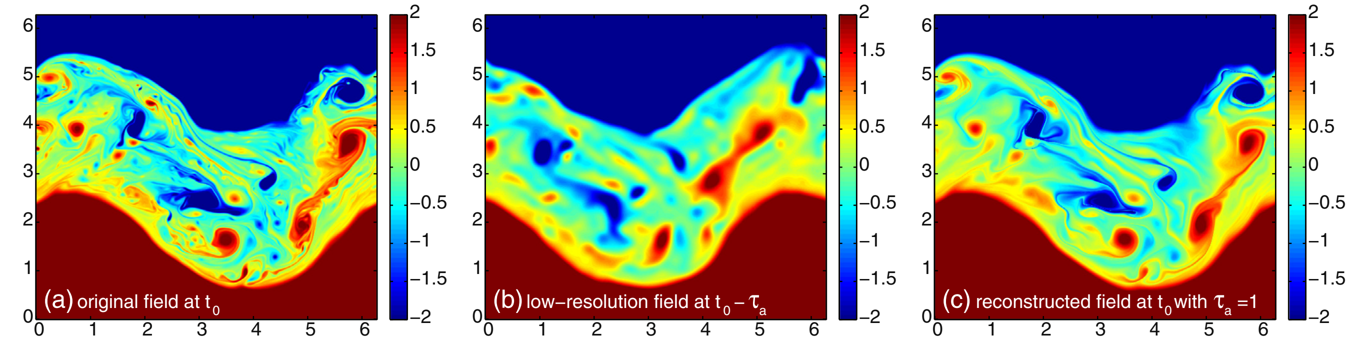

Fig. 3. Snapshots of SST: original field at time $t_0 = 50$ (a), low-resolution field for $\tau_a = 1$ (b), reconstructed field at t_0 for an advection time interval $\tau_a = 1$ (c).

The statistical description of the turbulent dynamics in this regime is given by the spectrum of temperature fluctuations $\theta'(\mathbf{x},t) \equiv \theta(\mathbf{x},t) - \langle\theta(\mathbf{x},t)\rangle_x$. Notice that, because of the SQG relationship $\mathcal{F}(\psi) = \mathcal{F}(\theta')/k$, it is identical to the spectrum of kinetic energy. The spectrum, time averaged during the statistically steady state, is reported in Fig. 6 (curve with circles). The scaling behavior is not far from $E_u(k) \sim k^{-2}$, that is slightly steeper than the $k^{-5/3}$ predicted by SQG theory (Held et al., 1995; Smith et al., 2001), but in agreement with 3D primitive-equation simulations at submesoscale (Capet et al., 2008; Klein et al., 2008).

A quantity of interest for the ensuing discussion is the typical timescale associated with the Eulerian flow, the eddy turnover time τ_E. One possible estimation of the latter is $\tau_E \approx \langle\zeta^2\rangle^{-1/2}$ where $\zeta = (\partial_x v - \partial_y u)$ is vorticity and $\langle\cdots\rangle$ indicates an average over the spatial domain. This definition provides a value of τ_E between 0.1 and 0.2. Alternatively, τ_E can be dimensionally estimated from the typical sizes and velocities of the largest eddies. This second definition provides a larger value $\tau_E \approx 0.35$.

4. Analysis and results

In this section we present the results of Lagrangian reconstructions. The tracer field that we aim to reconstruct is the total temperature field $C \equiv \Theta$. Before coming to the results it is useful to summarize the main settings and parameters used.

We proceed as follows. From the simulations described in Section 3 we build a time history of velocity and temperature fields $\mathbf{u}(\mathbf{x},t)$ and $\Theta(\mathbf{x},t)$, respectively, which are stored with a time interval $\Delta t = 0.1$. The value of the latter is chosen to be somewhat smaller than the characteristic time $\tau_E \approx 0.35$ associated with the dynamics of the largest eddies. It has been checked that the results are not too sensitive to the value of the time interval Δt. These fields are the high-resolution ($\delta x = 2\pi/N_{hr} \approx 0.012$ with $N_{hr} = 512$) data constituting our numerical "reality", with which we will compare the different reconstructions. In the following we will refer to them as $\mathbf{u}_{hr}$ and Θ_{hr}. Two procedures were tested to obtain from $\mathbf{u}_{hr}$ and Θ_{hr} the fields degraded at low-resolution $\mathbf{u}_{lr}$ and Θ_{lr}. In the first case we spectrally degrade the fields by elimination of all Fourier modes with wavenumber larger than a cut-off value k_d. In the second case, we apply a low-pass Butterworth filter (of order 3 and with a cut-off wavenumber equal to 20) to $\mathbf{u}_{hr}$ and Θ_{hr}, which operates a smoothing in physical space and leaves a smoothly decreasing spectrum beyond the wavenumber k_d. The two types of degradation procedure give similar results for comparable values of k_d and in the following we will present only the results for the smoothly degraded fields, which we expect to be more similar to those usually found in satellite data. Other cut-off scales were chosen and the results did not change qualitatively. Filtering provides low-resolution fields with an effective resolution of order $\Delta x = 16\pi/N_{hr} \approx 0.1$. Notice that this is similar to what happens in a realistic situation where satellite data are available at a resolution $\Delta x \approx 100$ km and one is interested in submesoscale features of size $\delta x \approx 10$ km.

Reconstructions are then performed to obtain the field Θ_{rec}, as described in Section 2, with a number $N_p \equiv N^2$ of particles. In order to ease the comparison we typically choose $N \equiv N_{hr} = 512$, but some calculations have been performed also with $N = 1024$ or $N = 2048$. Particles are advected backward in time by means of a 4th order Runge–Kutta algorithm with a time-step $\delta t = \Delta t/25$. Similar values of time-step ratios are used in observational studies (e.g., in Desprès et al. (2011a), where $\Delta t = 7$ days and $\delta t = 6$ h). At intermediate times between those where it is known, the low-resolution advecting velocity field is linearly interpolated. However, using a piecewise constant (in time) velocity does not dramatically change the results. The values of the fields $\Theta(\mathbf{x}_p,t)$ and $\mathbf{u}(\mathbf{x}_p,t)$ at the particle position $\mathbf{x}_p$ are obtained by bicubic spatial interpolation using the 16 neighboring points on the low-resolution grid.

In the following we will examine the reconstructed temperature field Θ_{rec} at a given instant of time t_0. The time t_0 is chosen in the statistically steady state of the SQG simulation and it has been checked that the results do not significantly depend on its value. We will then consider backward advection of trajectories until time $t_0 - \tau_a$ and we will vary τ_a to explore the sensitivity of reconstructions to this parameter. The values of τ_a will be compared to the eddy turnover time of the low-resolution velocity field, estimated as $\tau_{lr} \approx \langle\zeta_{lr}^2\rangle^{-1/2}$, where ζ_{lr} is vorticity. This time roughly corresponds to the typical timescale of structures of size comparable to k_d^{-1}; its value is $\tau_{lr} \approx 0.2$ in the present case. It is interesting to observe that such a quantity is accessible also from altimetry measurements.

Finally, let us mention that an important aspect of the present study is the fact that the tracer to reconstruct is not conserved, since it is forced by the relaxation term F in Eq. (5). Indeed, we are interested in assessing the capability of the reconstruction method in a situation where the conservation property of Θ is violated. Such a case is relevant for oceanographic applications where, typically, SST is not a passively transported quantity and, in general, it is hard to find a tracer field which evolves in the absence of any forcing mechanism.

4.1. Reconstruction of SST fields

In Fig. 3 we provide an example of how the technique works. Panel (a) shows a high-resolution field $\Theta_{hr}(\mathbf{x},t_0)$ at time $t_0 = 50$, which we aim to reconstruct. Here we choose to fix a time interval $\tau_a = 1$ for which the reconstruction will be performed (by backward advection up to $t_0 - \tau_a$). In the low-resolution field $\Theta_{lr}(\mathbf{x},t_0-\tau_a)$ at time $t_0 - \tau_a$, shown in panel (b), many small-scale features have disappeared, such as long and thin filamentary structures and small size vortices. Then we reconstruct the temperature field at time $t_0, \Theta_{rec}(\mathbf{x}, t_0; \tau_a)$, through our Lagrangian technique using the low-resolution temperature field $\Theta_{lr}(\mathbf{x}, t_0 - \tau_a)$ at time $t_0 - \tau_a$, panel (b), and the Lagrangian particles. By this method, we obtain panel (c) of Fig. 3, which shows the appearance of tracer small scales in the form of filaments. For comparison, the low resolution temperature field at time t_0 (corresponding to $\tau_a = 0$) is reported in Fig. 4b.

Considering reconstructions as a function of τ_a (as shown in Fig. 4) returns a more detailed picture. The advective timescale τ_a is the main parameter controlling the production of small scales, since increasing it corresponds to extend the tracer cascade to small scales. For small advection times, only a small amount of fine scales emerges (Fig. 4c). In the interval $5\tau_{lr} < \tau_a < 10\tau_{lr}$, with $\tau_{lr} = 0.2$, (Fig. 3c and Fig. 4d) we observe the best agreement between the original SST image (Fig. 4a) and the reconstructed ones. In this range of values of τ_a a conspicuous part of filamentary structures is recovered, namely those produced by the stretching induced by large-scale eddies. For $\tau_a = 7.5\tau_{lr}$ or close to it, the reconstructions work rather well and the similarity with Θ_{hr} is quite impressive by visual inspection (compare Fig. 4a and d). However, some differences can also be noticed, when looking at large-scale structures. The intensity of the latter is weaker than in the original field and it decreases as the advection time τ_a grows (see the vortex at $(x, y) \approx (0.25, 5)$ in Fig. 4, panels (c) to (f)). This effect is related to the fact that, in the reconstructions, SST is assumed to be a passive quantity; we will come back to this point at the end of the present section. For large enough advection times ($\tau_a > 10\tau_{lr}$) a sort of granularity spoils the reconstruction, with this phenomenon becoming more pronounced at increasing τ_a (see Fig. 4f). This is due to the absence of any dissipation mechanism, like diffusion, during advection of virtual particles, which produces an endless growth of small-scale gradients (Legras et al., 2005).

An interesting question we now want to address concerns the possibility to reconstruct thermal fronts. To identify fronts we compute the intensity of the gradient field, given by $|\nabla\theta'|$, which is shown in Fig. 5. The gradients of the original temperature field θ'_{hr} at t_0 are shown in panel (a), those of the low-resolution field at the same time in panel (b). In panel (c) we present the gradient field $|\nabla\theta'_{rec}(\mathbf{x}, t_0; \tau_a)|$ for a reconstruction with an advection time $\tau_a = 8\tau_{lr}$ within the interval previously estimated as optimal. Here, due to the fact that gradients are by definition small-scale quantities, the effect of low resolution is even more clearly visible than in Fig. 4b. Indeed, after filtering, nearly all small-scale structures have disappeared (see Fig. 5b). In the reconstructed field, on the other hand, a striking number of frontal structures are recovered. Despite some differences exist, filaments now bear a very good resemblance with those found in the original SST field. Consider, for instance, the front attached to the vortical structure centered in the vicinity of the point $(x, y) = (4.5, 3)$, which had practically disappeared after filtering, or the elongated double-vortex structure extending from about (5, 1.5) to about (5.5, 3.5), which is absent in the low-resolution field.

It is worth to remark, here, that the dynamics of the gradients of a tracer conserved along Lagrangian trajectories is tightly related to the concept of Finite Time Lyapunov Exponent (FTLE) (Crisanti et al., 1991). This is due to the strong similarity between the evolution equation for the tracer gradient and that for a small displacement $\boldsymbol{\delta} = \mathbf{x}_2 - \mathbf{x}_1$ between two trajectories $\mathbf{x}_1(t)$ and $\mathbf{x}_2(t)$. Indeed, both evolutions are essentially governed by the velocity gradient tensor. As a consequence, the images shown in Fig. 5 could also be interpreted as maps of FTLE (see also Lapeyre, 2002).

So far we have presented qualitative comparisons, as in the majority of studies devoted to the issue of improving low-resolution oceanographic data. In order to get a more quantitative characterization of their effectiveness, we now turn to the statistical properties of reconstructions.

In Fig. 6 we report the horizontal wavenumber spectra of the reconstructed temperature perturbations (without zonal mean) θ', with an advection time interval $\tau_a = 8\tau_{lr}$, for three different resolutions $N = 512, 1024, 2048$. In the figure we also show the spectra computed from the original (black circles) and the low-resolution (black crosses) fields at $t_0 = 50$. Here the effect of filtering is well evident: beyond $k_d \simeq (20 - 30)$, the spectrum of the low-resolution field steeply decreases due to the elimination of small scales, while at scales larger than k_d^{-1} it is indistinguishable from that of the original field θ'_{hr}. The reconstruction procedure allows

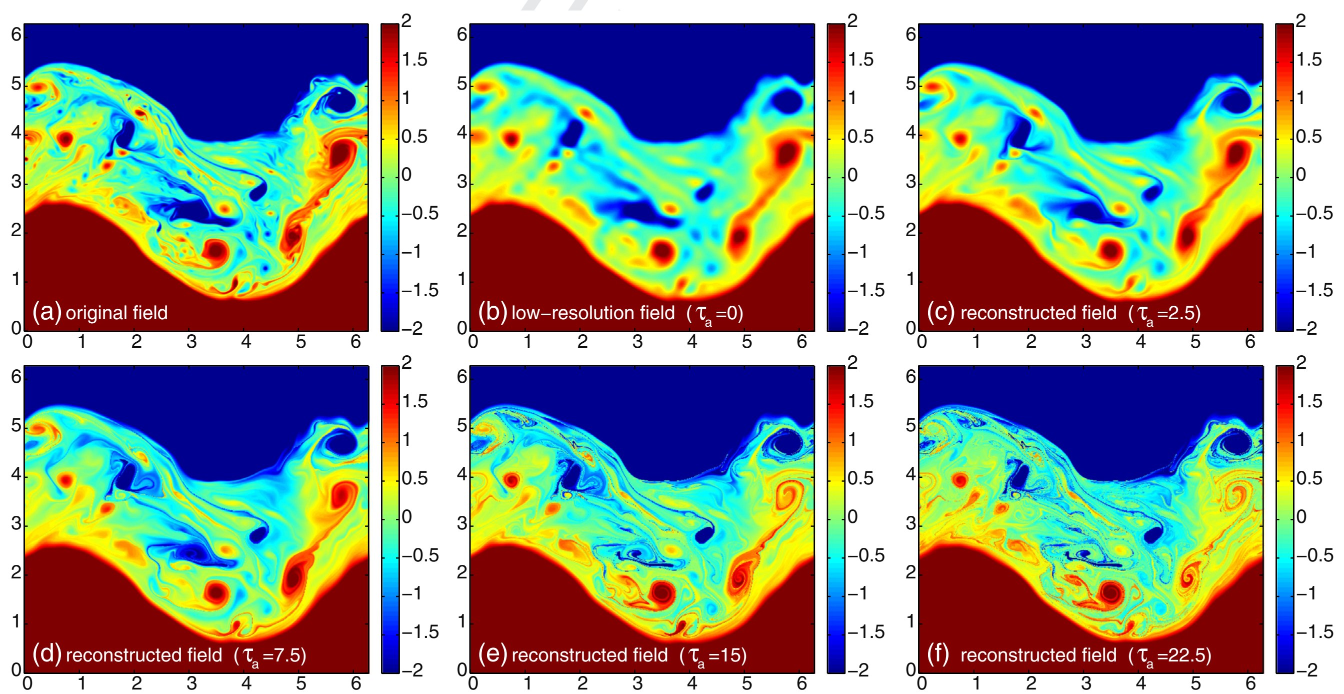

Fig. 4. Snapshots of SST: original field at time $t_0 = 50$ (a); reconstructed field for different values of $\tau_a = 0, 2.5, 7.5, 15, 22.5$ (in units of $\tau_{lr} = 0.2$), panels (b) to (f). The advection time $\tau_a = 0$ corresponds to the low-resolution field.

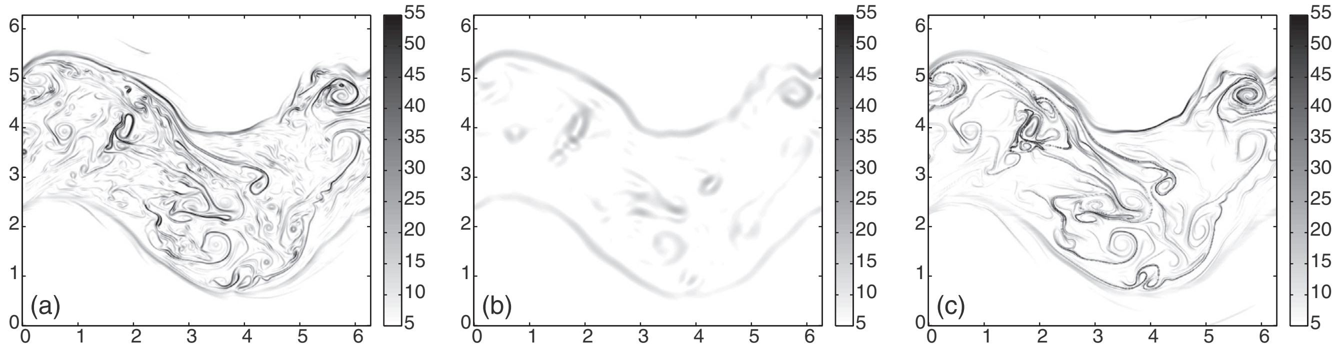

Fig. 5. Intensity of temperature gradients $|\nabla\theta'|$: original field at time t_0 (a), low-resolution field at the same time (b), reconstructed field at t_0 for $\tau_a = 8\tau_{lr}$ (c).

to smoothly extend the spectrum at wavenumbers $k > k_d$. In other words, the small-scale energetic content is progressively rebuilt when increasing the duration of reconstruction. This reflects the cascade of tracer variance to small scales which is associated with the chaotic advection of our synthetic Lagrangian particles and demonstrates the presence of small-scale features in the reconstructions. The logarithmic slope of the spectrum is close to that obtained from the original field, for reconstructions with $\tau_a = 8\tau_{lr}$. Interestingly, this advection time belongs to the interval $5\tau_{lr} < \tau_a < 10\tau_{lr}$, for which we already found that the similarity of Θ_{hr} and its reconstruction is most evident. The energy content at the smallest scales grows with τ_a and accumulates at the highest wavenumbers. We remark that this is not a physical effect, but rather a numerical one, directly related to the granularity of reconstructions seen in Fig. 4 for large τ_a. Because no small-scale dissipation is present, energy piles up at the largest wavenumber, due to limited resolution. Indeed, when reconstructions are performed with a larger number of particles, that is at higher spatial resolution ($N = 1024$ and $N = 2048$), the power law scaling range is extended (see Fig. 6).

The statistics of thermal fronts is quantified by the probability density function (PDF) of SST gradients. In Fig. 7 we compare the gradients PDF $P(|\nabla\theta'|)$ for the original field (black triangles) and for reconstructions (thin gray lines) at several advection time intervals τ_a increasing of $\Delta\tau_a = 0.5 = 2.5\tau_{lr}$ from inside out. The thick red line refers to advection with $\tau_a = 8\tau_{lr}$, corresponding to a gradient field like the one in Fig. 5c. The statistics of gradients computed on the original field are markedly non-Gaussian (as it can be deduced from $P(\partial_y\theta')$ shown in Fig. 7b, or $P(\partial_x\theta')$ which gives analogous results), as is typical in turbulent flows. The high tails of the PDFs correspond to high frequencies of extreme events, in this case very intense fronts. The probability distributions computed on the reconstructed fields are close to Gaussian for short advection times but they soon depart from this behavior developing higher and higher tails, when τ_a is increased. This indicates a progressive increase in the abundance of strong gradients, a typical manifestation of the tracer cascade to small scales. As already discussed, the production of fine scales does not stop, due to the absence of dissipation, and for large values of τ_a leads to an excess of intense gradients. We observe that for advection times in the interval $5\tau_{lr} < \tau_a < 10\tau_{lr}$, in particular for $\tau_a = 8\tau_{lr}$, the PDFs of SST gradients of the reconstructed field are remarkably close to those of the original field (compare the thick red curve with the black triangles in the figure). The good agreement indicates the potential of the Lagrangian reconstruction technique for the reproduction of the statistical features of fronts. Moreover, it gives us a further estimation of an optimal reconstruction duration $\tau_a = 8\tau_{lr}$, in reasonable agreement with what previously found.

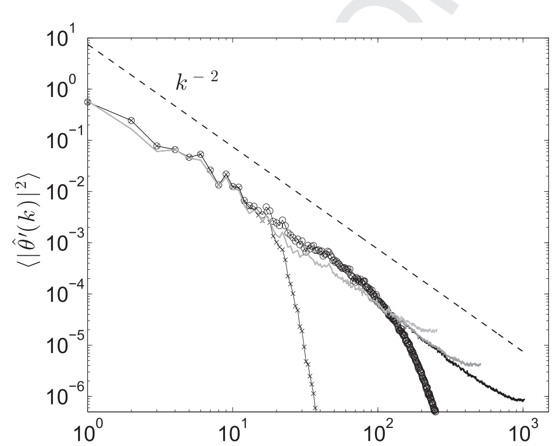

Fig. 6. Power spectrum of SST fluctuations $\theta' = \theta - \langle\theta\rangle_x$. Circles correspond to the spectrum of the original field, crosses to that of the low-resolution field. The thin gray lines are for $N = 512, 1024, 2048$ (from lighter to darker) with $\tau_a = 8\tau_{lr}$.

Having assessed the quality of reconstructions in a statistical sense, it is then interesting to see how they perform at some specific locations. For this purpose we now consider transects of the full SST field $\Theta = \theta + \beta y$. In Fig. 8 we show a meridional section at half width of the domain ($x_* = \pi$), going from $y = 1.75$ to $y = 4.25$ (for $t_0 = 50$); similar results are obtained for different transects, both in the meridional and in the zonal directions, and for other values of t_0. The figure presents a comparison between the original SST (black curve) and the reconstructed one (red curve); the duration of advection is $\tau_a = (0, 5, 7.5, 10)\tau_{lr}$ in panels (a) to (d), respectively; recall, also, that $\tau_a = 0$ corresponds to the low-resolution field at t_0. The following features can be observed. For the low-resolution field (Fig. 8a), as expected, we find the correct large-scale structure; however it is apparent that this field is considerably smoothed, as small-scale gradients are no longer present. In the reconstructed SST, on the other hand, the latter gradually reemerge with increasing τ_a (Fig. 8b–d) as a consequence of the chaotic advection of virtual particles. Interestingly, even rather steep gradients are found in the reconstructions, but part of them is slightly displaced with respect to the correct position in the "real" high-resolution field Θ_{hr} (e.g., the sharp front at $y \approx 3.9$ in Fig. 8c). It is worth to notice that the same problem was found in observations of submesoscale filaments (Legras et al., 2005; Mariotti et al., 1997; Desprès et al., 2011a). For τ_a large enough, more and more small scales can be seen, but the agreement with the original SST gets worse (Fig. 8d). As already pointed out, these are unphysical gradients produced by the cascade of tracer variance (associated with the reconstruction procedure) in the absence of diffusion. Finally, as also seen in Fig. 4c–f, some differences are found at large scales; for instance, in correspondence of the low temperature vortex centered in $(x, y) = (\pi, 2.5)$

Q1 Please cite this article in press as: Berti, S., Lapeyre, G. Lagrangian reconstructions of temperature and velocity in a model of surface ocean turbulence. Ocean Modell. (2014), http://dx.doi.org/10.1016/j.ocemod.2014.02.003

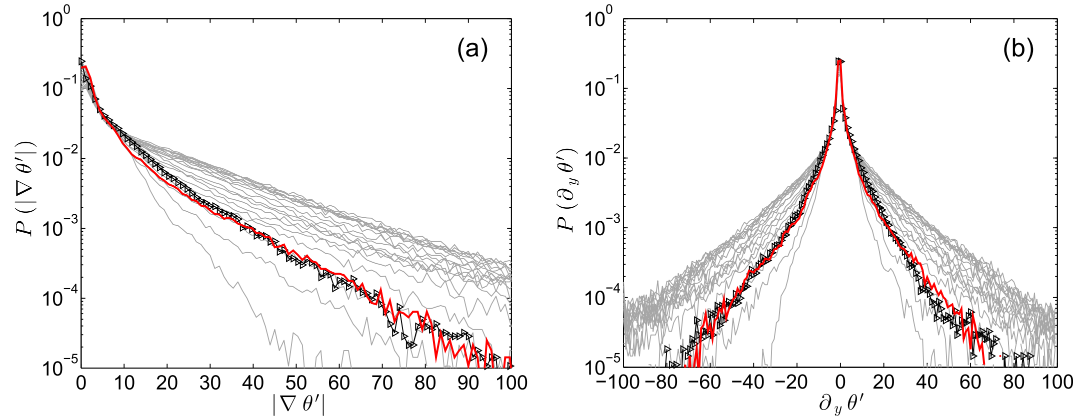

Fig. 7. PDFs of the magnitude (a) and of the meridional component (b) of SST gradients at various advection times $\tau_a = 2.5, 5, 7.5, \ldots, 50$ (in units of $\tau_{lr} = 0.2$) from inside out (gray curves). Triangles correspond to PDFs computed with the original field, the thick red curve is for a reconstruction with $\tau_a = 8\tau_{lr}$. (For interpretation of the references to colour in this figure caption, the reader is referred to the web version of this article.)

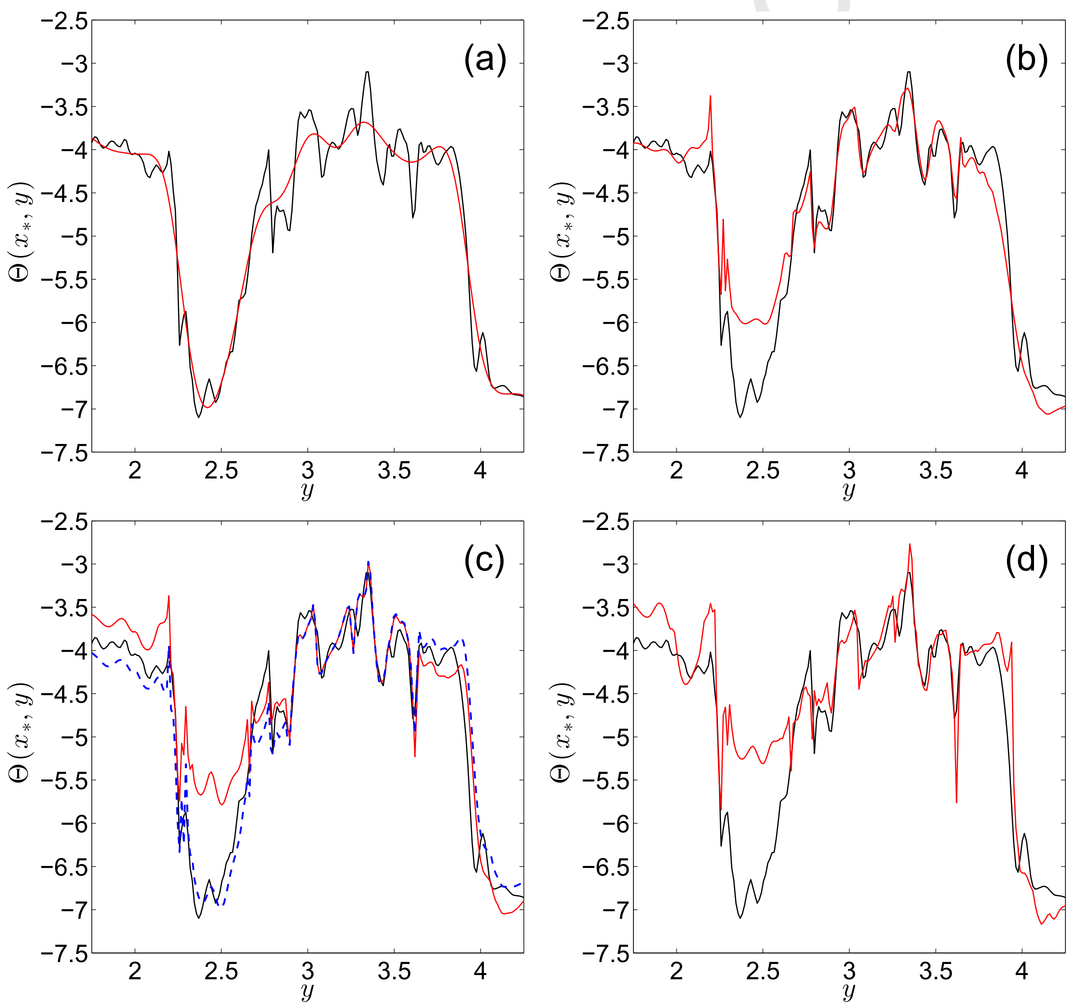

Fig. 8. Meridional transects of SST at half width ($x_* = \pi$) of the spatial domain, for $\tau_a = 0, 5, 7.5, 10$ (in units of $\tau_{lr} = 0.2$), panels (a) to (d). The black lines are for the original field, the red ones for the reconstructions. Notice that $\tau_a = 0$, panel (a), is the same as considering the low-resolution field. In panel (c), the dashed blue line is for the reconstruction taking into account the forcing. (For interpretation of the references to colour in this figure caption, the reader is referred to the web version of this article.)

the magnitude of the reconstructed SST decreases when τ_a is increased.

This last remark leads us to comment on the role of the forcing. Despite many reconstructed structures are found in the correct place, their intensity is not always appropriate. This feature is more prominent at large scales. For instance, as it can be seen in Fig. 4, a continuous reduction with τ_a is visible in the intensity of a warm vortex and a thick filament located close to $(x, y) = (5.7, 4)$. The reason for this type of mismatch can be traced back to the non-conservative nature of the field Θ. Indeed, while SST is

Q1 Please cite this article in press as: Berti, S., Lapeyre, G. Lagrangian reconstructions of temperature and velocity in a model of surface ocean turbulence. Ocean Modell. (2014), http://dx.doi.org/10.1016/j.ocemod.2014.02.003

passively transported in the Lagrangian reconstructions, in the Eulerian simulations the term $F = -\kappa(\langle\theta\rangle_x - \bar{\theta})$ provides a (large-scale) mechanism which forces it to continuously relax to the unstable temperature profile. Let us recall that the latter is nonzero only in two strips centered around $y_1 \simeq 2$ and $y_2 \simeq 4$. The lack of intensity originates at short advection times from these strips, where the relaxation to the profile $\bar{\theta}$ is most effective, and then propagates into larger portions of the spatial domain. We carried out reconstructions taking into account the action of the forcing by means of an algorithm (described in the Appendix A) based on the discrete time approximation of the "reactive" dynamics induced by F. This way it was possible to compensate, at least to some extent, the reduction of intensity. Cross sections at $x_* = \pi$ confirm this: when the forcing is included in the reconstruction algorithm the agreement with the profile of the original SST is improved, as it can be seen in Fig. 8c (compare the red and the dashed blue curves with the black one). This effect is more relevant in the neighborhood of large-scale structures, as the aforementioned vortex at $(x, y) = (\pi, 2.5)$.

4.2. Reconstruction of the flow field

A strong advantage of the SQG framework described in Section 3 is the possibility to retrieve the full velocity field, as a function of depth, from surface information alone, namely from the knowledge of the surface buoyancy (or temperature) field. Using the hypothesis of uniform quasi-geostrophic potential vorticity (see Lapeyre and Klein, 2006, for details), one can derive from this theory that the streamfunction ψ is strongly correlated to the surface temperature θ. At the surface the relation between the two reads

$$\mathcal{F}(\psi) = \frac{\mathcal{F}(\theta)}{k}, \tag{9}$$

in Fourier space, where $\mathcal{F}()$ is the direct Fourier transform, $\mathbf{k}$ is the horizontal wavevector and $k \equiv |\mathbf{k}|$. From Eq. (9), after performing the inverse Fourier transform, the horizontal flow is easily calculated as $(u, v) = (-\partial_y\psi, \partial_x\psi)$.

As a consequence of the uniform PV hypothesis, in this model horizontal and vertical structures of the flow are related to each other. In order to take into account three-dimensional effects, an interesting quantity to consider is the ageostrophic divergence, which is tightly linked to the vertical velocity. The surface ageostrophic divergence field D can be calculated starting from the geostrophic variables (see e.g., Hakim et al., 2002). In non-dimensional units, this gives

$$D = -\nabla \cdot \{\mathbf{u}\zeta + \mathcal{G}(k\mathcal{F}(\mathbf{u}\theta))\}, \tag{10}$$

where $\zeta = (\partial_x v - \partial_y u) = \nabla^2\psi$ is vorticity and $\mathcal{G}()$ stands for the inverse Fourier transform.

Therefore, once the small-scale surface temperature has been reconstructed through the Lagrangian technique, it is in principle possible (using the SQG formalism) to reconstruct the flow field, too. From the streamfunction, the vorticity and ageostrophic divergence fields, respectively accounting for horizontal and vertical motions, can be derived as discussed above. In Fig. 9 we present the vorticity ζ for the high-resolution field at $t_0 = 50$, the low-resolution one at the same time, and a reconstruction with $\tau_a = 6.5\tau_{lr}$. For this advection time we observe the best agreement between the original and reconstructed fields; results with $\tau_a = 8\tau_{lr}$ are similar, apart from the presence of smaller scales. In the high-resolution field (Fig. 9a) very large values of vorticity are found in large-scale eddies, but also in small-scale structures (both filaments and eddies). This is a main difference with respect to temperature (Fig. 3a), since vortices capture most of the SST anomalies. As a result, vorticity is contained in a variety of scales. The low-resolution field (Fig. 9b) is much weaker in magnitude (about one half). In comparison with temperature (Fig. 4b), the vorticity contours associated with large-scale eddies are now blurred, and filaments are almost not visible. On the other hand the reconstructed field (Fig. 9c) possesses numerous and intense vorticity structures at fine scales, which were present also in its high-resolution counterpart. However, many submesoscale vorticity anomalies are missed by the reconstruction (for instance the small-scale eddies near $(x, y) = (3, 3)$) and part of the space is empty of structures. This corresponds in general to filaments that roll up in small eddies. Hence, reconstructions permit to recover several submesoscale dynamical structures, but only those corresponding to almost elongated fronts.

The ageostrophic divergence D shown in Fig. 10a is dominated by submesoscales with very patchy patterns. Some structures are nonetheless visible, and they are consistent with what was observed in realistic simulations (Lévy et al., 2001). Filaments are associated with convergence and divergence across them caused by frontogenesis (see the filament at $(x, y) \approx (5.5, 2.5)$). Vortices are associated with quadrupolar patterns in divergence, such as the eddies at $(x, y) \approx (1.8, 4)$ and $(x, y) \approx (4.2, 3)$. These are induced by the curvature variation of the flow that impacts the stretching of temperature fronts and the divergence associated with subsequent frontogenesis. The low-resolution divergence only displays large scales with weak intensity (Fig. 10b). Except for some quadrupolar patterns (like those corresponding to the two eddies previously mentioned), only very few and broad filaments are visible. In the reconstructed field with $\tau_a = 6.5\tau_{lr}$ (Fig. 10c) significantly more submesoscales with high values of divergence are found. Many of them are present in the original field as well, but many others are missing, as evidenced by the empty regions in the figure. This confirms what was already observed for vorticity, namely that the reconstruction is essentially unable to recover small-scale eddies and their dynamics.

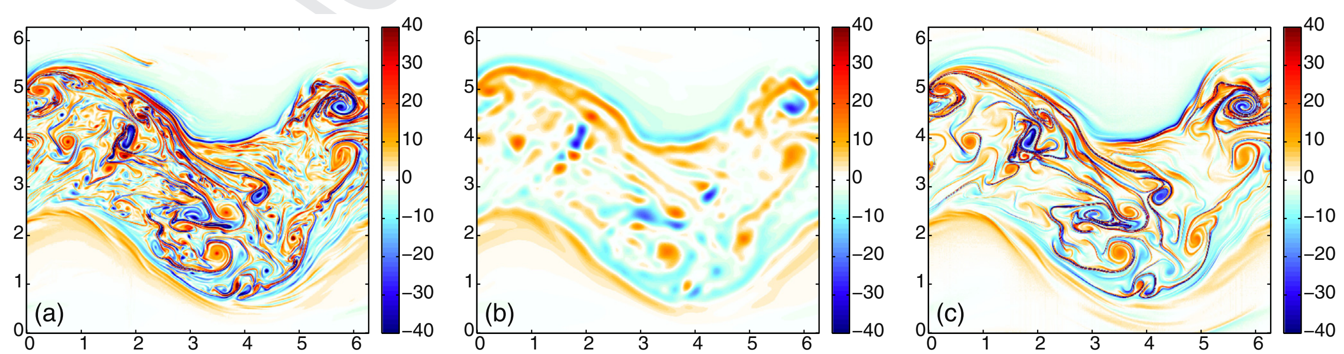

Fig. 9. Vorticity at the surface for the original field (a), the low-resolution field (b), the reconstructed field with $\tau_a = 6.5\tau_{lr}$ (c).

Q1 Please cite this article in press as: Berti, S., Lapeyre, G. Lagrangian reconstructions of temperature and velocity in a model of surface ocean turbulence. Ocean Modell. (2014), http://dx.doi.org/10.1016/j.ocemod.2014.02.003

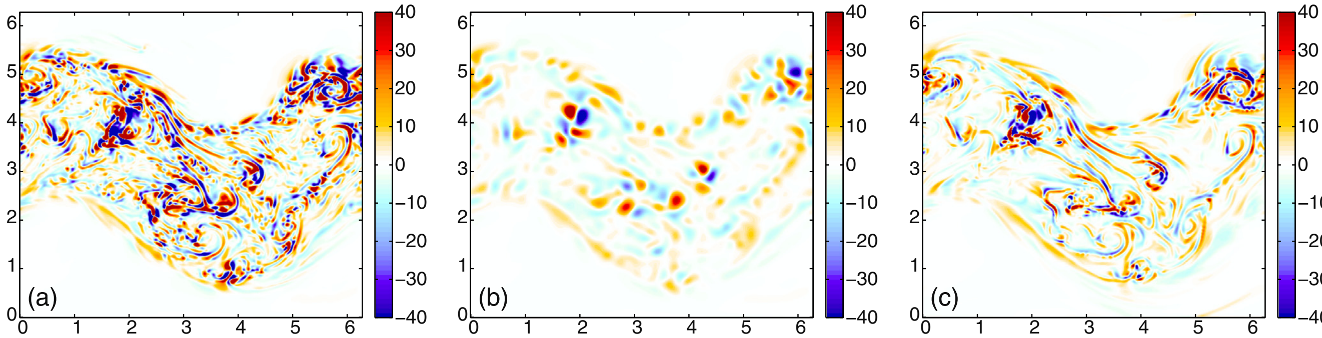

Fig. 10. Ageostrophic divergence at the surface for the original field (a), the low-resolution field, the reconstructed field with $\tau_a = 6.5\tau_{lr}$ (c).

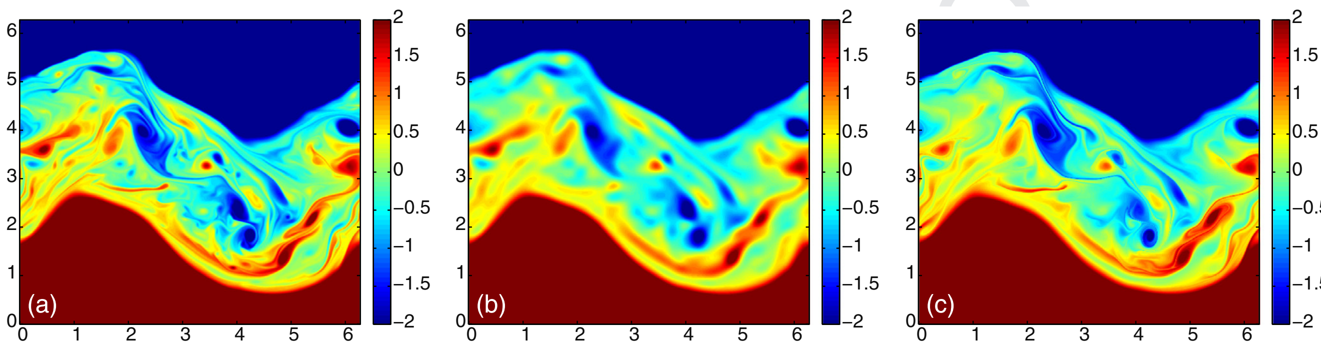

Fig. 11. Snapshots of SST: original field (a), low-resolution field (b), reconstructed field for an advection time interval $\tau_a = 6.5\tau_{lr}$ (c). Simulation with enhanced dissipation ($k_c = 1$).

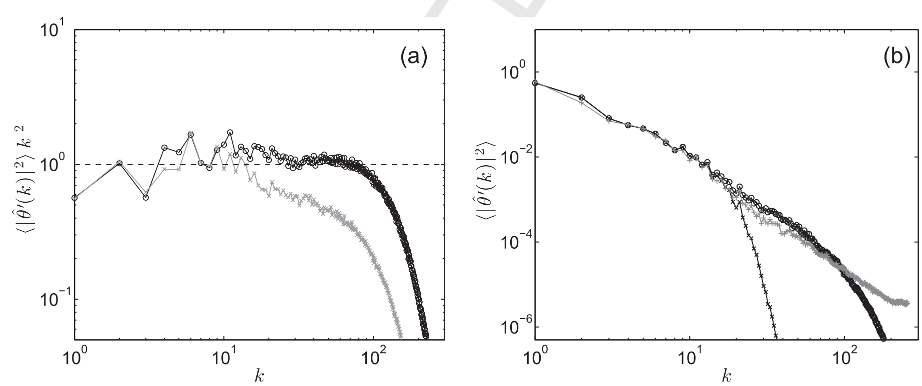

Fig. 12. (a) Power spectra of high-resolution SST fluctuations compensated by k^{-2} for simulations with $k_c = 40$ (black circles) and $k_c = 1$ (gray crosses). The dashed line is a reference to a constant. (b) Power spectra of SST fluctuations for the $k_c = 1$ case: black circles correspond to the high-resolution field and black crosses to the low-resolution one. The gray crosses correspond to a reconstruction of SST with $\tau_a = 6.5\tau_{lr}$.

5. Effects of nonlocality

An important point for the possibility to reconstruct the temperature field at small scales is that the velocity field is mainly governed by large scales (see e.g., Methven and Hoskins, 1999; Bartello, 2000; Keating et al., 2011). In that situation there is a clear scale separation between the advecting features responsible for the stretching of filaments, and the filaments not contributing to their own stretching. The corresponding flows are considered "non-local" and this is the case when the kinetic energy spectrum is steeper than k^{-3}. The production of small scales is then primarily driven by the large-scale stretching, i.e., those scales at the top of the k^{-3} (or steeper) range. In the method we propose, reconstructions are necessarily non-local because, after filtering, the kinetic energy spectrum is much steeper than k^{-3} beyond the cut-off wavenumber k_d (see Fig. 6). As a result, the most relevant scale for small-scale advection is given by the smallest resolved one (k_d^{-1}).

However, SQG flows are considered "local" as the kinetic energy spectrum is predicted to be in $k^{-5/3}$ and because of the formation of vortices at any scales (see e.g., Held et al., 1995). In this case dispersion processes should be substantially affected by the structure of the velocity field at different scales. The analysis carried out in the previous section indicates that it is still possible to reconstruct a relevant part of the small-scale temperature field, even if this result appears to contradict our thinking about locality. A close inspection of the temperature gradients (Fig. 5a and c) or the vorticity field (Fig. 9a and c) actually reveals that small-scale vortices

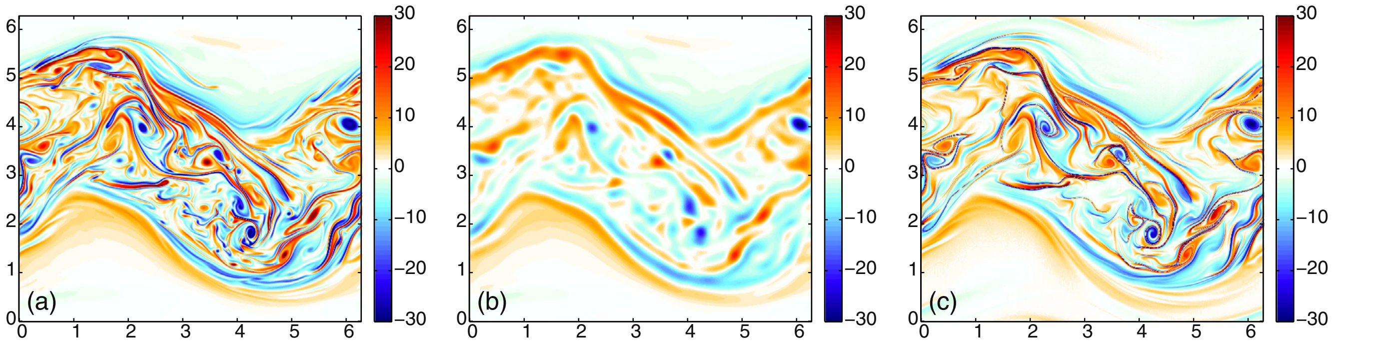

Fig. 13. Vorticity at the surface for the original field (a), the low-resolution field (b), the reconstructed field with $\tau_a = 6.5\tau_{lr}$ (c). Simulation with enhanced dissipation ($k_c = 1$).

are present in the high resolution field but are completely absent in the reconstruction. Therefore our results are not in contradiction with locality arguments. Indeed, they show that only filaments produced by the stirring of large-scale eddies can be retrieved by our method. The production of small scales is due to both small-scale eddies and larger ones and, depending on the flow properties, one will be more important than the other.

Scott (2006) investigated the transition from locality to nonlocality by examining the behavior of a passive tracer advected by a velocity field coming from a SQG simulation and taken at different depths. In this case, the different flows have steeper spectra when depth increases. He found that a non-local behavior occurs for steep spectra. To examine in our experiment if reconstructions improve for steeper energy spectra, we repeated the reconstruction procedure using a flow in the same configuration as in Section 3 but with a cut-off wavenumber $k_c = 1$ (instead of $k_c = 40$). The resulting flow is smoother, i.e., its kinetic energy spectrum is steeper (see Fig. 12a), which should be more appropriate for non-local dynamics. The eddy turnover time of the corresponding low-resolution velocity field is rather close to the value $\tau_{lr} = 0.2$ already found for $k_c = 40$. Filaments associated with the stretching of large-scale eddies are still abundant, but the population of small-scale vortices is substantially reduced (Fig. 11a). Small-scale filaments that were absent in the low-resolution field (Fig. 11b) are now apparent in the temperature reconstruction (Fig. 11c). The quality of the reconstruction seems better than for the reference case $k_c = 40$. Spectra of temperature perturbations are shown in Fig. 12b for the original field at a fixed time, the low-resolution one at the same time and a reconstruction with a duration of advection $\tau_a = 6.5\tau_{lr}$. Similarly to the previously examined case ($k_c = 40$) the advection time interval appears to be optimal for values of order few τ_{lr}, though now its value is likely a little smaller.

The computations of vorticity and divergence for this flow are presented in Figs. 13 and 14. The observed behavior is the same as in the reference case, namely the small scales that can be reconstructed correspond to filaments associated with large-scale eddies. This shows that, as long as one is concerned with this type of structures, the local dynamics of small eddies does not prevent the possibility to reconstruct them. However, from a quantitative point of view small eddies certainly have an impact. To characterize their role we measured an error based on temperature or on vorticity, the last being an appropriate indicator of small-scale content. The error is calculated as follows. First, the spectrum of the difference between the temperature (vorticity) of the high-resolution field and that of a reconstruction with a given advection time τ_a is computed, after removing a large-scale gradient with a least squares method. Then, the normalized variance of this quantity in the wavenumber interval $20 < k < 100$ (corresponding to the range of scales to be reconstructed) is computed as a function of τ_a. The normalization factor corresponds to the variance of the original field in the considered wavenumber interval. The results are shown in Fig. 15 (panel (a) for temperature and (b) for vorticity). In both cases, the error is found to be smaller for the flow with $k_c = 1$, as expected considering that in this case small-scale eddies are dynamically less important. Moreover, the error is larger for vorticity (Fig. 15b), which also indicates that a major factor limiting the quality of reconstructions at small scales is the presence of intense eddies governed by local dynamics, which cannot be captured by the advection of virtual particles by the largest structures.

The behavior of the error as a function of the advection time is in both cases characterized by a minimum for τ_a equal to few τ_{lr}, specifically τ_a between $4\tau_{lr}$ and $5\tau_{lr}$, for both $k_c = 40$ and $k_c = 1$. Though the error reduction is not very large, the decrease is clearly measurable. The value of τ_a corresponding to the minimum is not far from the advection time estimated as optimal in Section 4.1, but a little smaller. In this regard, however, it should be noted that the precise value of such an optimal time depends on the indicator

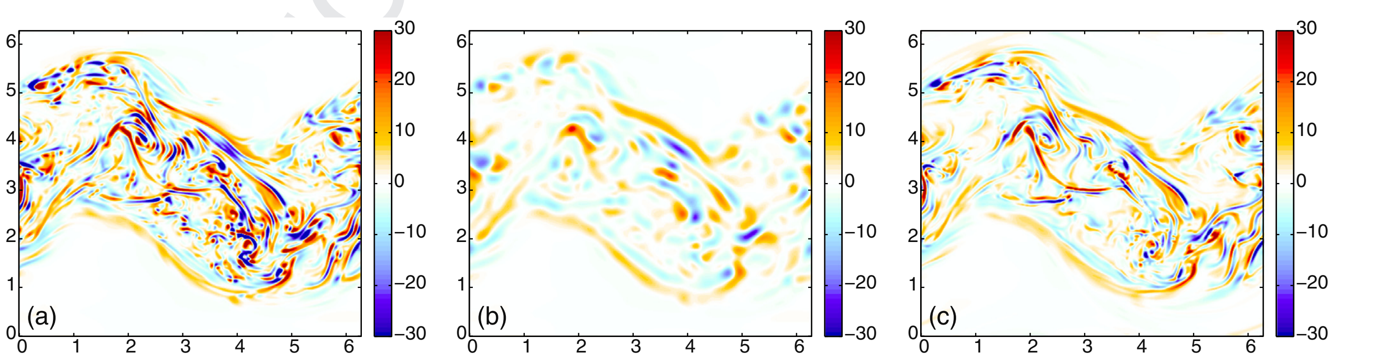

Fig. 14. Ageostrophic divergence at the surface for the original field (a), the low-resolution field (b), the reconstructed field with $\tau_a = 6.5\tau_{lr}$ (c). Simulation with enhanced dissipation ($k_c = 1$).

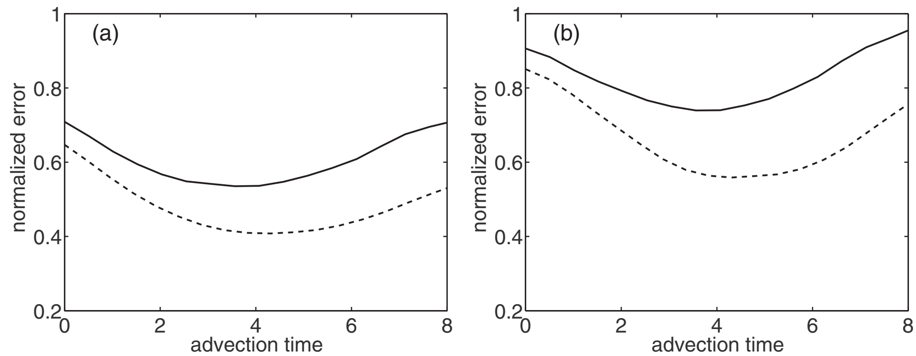

Fig. 15. Normalized error computed from (a) temperature and (b) vorticity. Continuous lines correspond to the simulation with $k_c = 40$ and dashed lines to the simulation with $k_c = 1$. Time is measured in units of the eddy-turnover time $\tau_{lr} = 0.2$.

chosen. For what concerns the divergence, hence the vertical velocity, the overall picture is the same, except that the minimum is found for smaller values of τ_a and that its value is larger, that is the error stays larger (not shown).

6. Discussion and conclusions

In this study we have considered Lagrangian reconstructions at the surface of the ocean. The method we used relies on the possibility to generate fine scales of a conserved quantity, like a passively transported tracer, by means of advection. In a nutshell, it consists in advecting a large number of synthetic particles with a given velocity field and in assigning to their final positions the value of the tracer at the origin of their trajectories, assuming tracer conservation. This way it is possible to use the information contained in a time series, at low resolution, of the tracer field and, in principle, to recover its small-scale features in space.

We have investigated the usefulness of this technique in the case of a turbulent SQG flow which resembles, in its main features, real oceanographic systems at mesoscale and submesoscale. The flow configuration consists of a westerly meandering jet in the presence of a large-scale mean temperature gradient. An important point of our study is that the dynamics of SST is forced by means of a relaxation to an unstable temperature profile. Clearly, such a situation is relevant in view of applications of Lagrangian reconstructions to realistic conditions, where the temperature at the surface of the ocean is not exactly conserved but, instead, is subject to air-sea forcing for instance.

We further addressed the possibility to extend the Lagrangian technique to reconstruct the flow field itself. This is an issue of great importance in consideration of studies aimed at the characterization of the dynamics of oceanic submesoscales. The reconstruction of the full 3D velocity field has been carried out by coupling the Lagrangian method with SQG theory. In this theory, a strong dynamical link exists between temperature at the surface and the streamfunction which accounts for the horizontal geostrophic flow. Moreover, it is possible to obtain the ageostrophic divergence, which is related to the vertical flow (Hakim et al., 2002; Lapeyre and Klein, 2006).

Inspection of the images resulting from the Lagrangian method reveals an overall agreement between the spatial patterns of the original high-resolution fields and their reconstructions. However the intensity of the reconstructed structures is not always correct, due to the absence of forcing in the Lagrangian procedure. As a consequence, reconstruction at large scales is limited by the role of the forcing, which is most effective in this range of scales, as also confirmed by reconstructions in which we take into account its presence by means of a modified algorithm. Nevertheless the forcing does not impact too much the reconstruction and this is likely due to its slower timescale ($1/\kappa = 3 = 15\tau_{lr}$) compared to the time for best reconstruction ($\tau_a \approx 1.5 = 7.5\tau_{lr}$).

The main characteristics of reconstructions are most evident when looking at physical quantities that better represent the small scales, like the gradients of SST, or the surface vorticity. Here it is seen that the filamentary structures associated with the stretching by large-scale eddies are well reproduced, although slightly shifted in space. This is an important result, due to the relevance of such structures for fluid dynamical as well as biogeochemical aspects. Moreover, concerning the statistics of thermal fronts, the results indicate a good agreement between the probability distribution of SST gradients in the original and reconstructed fields in a narrow range of reconstruction time intervals.

By comparing the images of gradient fields (of temperature as well as of velocity, namely vorticity and divergence) it is nonetheless apparent that the agreement is essentially limited to filaments produced by large eddies. Indeed, not all small scales are reproduced, particularly small intense eddies are absent in the reconstructions. This feature can be understood by noticing that the turbulent advecting flow is non-smooth and characterized by a quite flat spectrum $E_u(k) \sim k^{-2}$, some factors which have been shown, e.g., by Bartello (2000) and Keating et al. (2011), to limit the effectiveness of reconstructions in terms of virtual particles, due to locality of relative dispersion in this regime. We remark, at this regard, that the agreement found in our study refers to fine scales produced by the deformation field at large scales, and that small-scale vortices cannot be, and indeed are not, captured through the present Lagrangian method. Interestingly, the presence of such vortices does not prevent the reconstruction of the submesoscale associated with large eddies, at least from a qualitative point of view. However, comparing these results with those obtained with a flow possessing less intense small eddies and a steeper spectrum, we showed that this has a quantitative effect on the quality of reconstructions. This was quantified by measuring a relative error based on temperature and vorticity. Our results show that this quantity is smaller for the case in which small-scale eddies are dynamically less important. For both flow types the error reaches a minimum for advection times τ_a between 4 and 5, in units of the eddy turnover time $\tau_{lr} = 0.2$, suggesting this could be an optimal value for the reconstruction procedure.

The value of the optimal advection time deduced from the reconstructions of the flow is in reasonable agreement with that found from the analysis of the reconstructed SST images and related statistical quantities, like the spectrum of temperature fluctuations or the probability distribution of thermal fronts. As a way of comparison with a realistic situation, where $\tau_{lr} \approx 5$ days, using an estimate based on a mean strain rate $\gamma \approx 0.2$ days^{-1} which appears reasonable in regions of intense mesoscale activity (Waugh and Abraham, 2008), let us observe that the present result would imply an optimal reconstruction time between 20 days and a month. This

Q1 Please cite this article in press as: Berti, S., Lapeyre, G. Lagrangian reconstructions of temperature and velocity in a model of surface ocean turbulence. Ocean Modell. (2014), http://dx.doi.org/10.1016/j.ocemod.2014.02.003

estimate is quite close to the value of 30 days found in observational studies (Desprès et al., 2011a), but actually a little smaller. However two remarks are in order. First, the precise value of the optimal time depends on the indicator chosen. Second, several definitions of τ_{lr} are possible, which also affect the comparison. Nevertheless, the order of magnitude provided by the present study supports the value found in observational data.

To conclude, our analysis shows that Lagrangian methods are suited to reconstruct certain, but not all, characteristics of oceanic flows, for both tracer fields and three-dimensional currents. In particular they may be useful to reveal submesoscale filaments produced by mesoscale eddies, as well as to reproduce some statistical features like the distribution of thermal fronts. The coupling with SQG formalism appears to be an interesting tool permitting to access the three-dimensional structure of the flow, at least to some extent. Remark that, though the approach is here tested with SQG dynamics, it is more general and can be equally applied to other flow models. Nevertheless, from a quantitative point of view the agreement that can be obtained in a realistic configuration is limited. Oceanographic applications demanding quantitative estimations and detailed predictions at specific locations should then be considered with some caution. Indeed, as it has been shown, Lagrangian reconstructions in the ocean might be delicate due to two main factors: the forcing on the transported tracer, e.g., SST, and the dynamical role of intense small scales. Future developments should be directed to taking into account these aspects, in order to retrieve more and more quantitative information on submesoscale processes. This study is a first step as the validation was carried out in a controlled situation. It remains to be proven that the method can be used with real satellite images. We expect it to be more successful in regions (like the Gulf of Mexico and the eastern Nordic Seas) where the analysis of surface drifters data (LaCasce and Ohlmann, 2003; Koszalka et al., 2009) revealed non-local dispersion below the deformation radius.

Acknowledgments

We acknowledge interesting discussions with Francesco d'Ovidio and Marina Lévy and we are grateful to Patrice Klein and Massimo Cencini for useful comments. We would also like to thank two referees who helped improving the manuscript with their critical remarks. SB acknowledges financial support from CNRS, and from CNES during the second part of this work. GL acknowledges financial support from Agence Nationale de la Recherche under the reference ANR-09-Blan-0365-03.

Appendix A. Lagrangian reconstructions with forcing

The numerical method we used for including the forcing in the reconstructions is an adaptation of a pseudo-Lagrangian algorithm developed in Abel et al. (2001) to study the propagation of fronts in reaction–diffusion systems in terms of discrete-time maps. Let us recall that we are interested in the tracer $\Theta(\mathbf{x},t) = \theta(\mathbf{x},t) + \beta y$. The evolution of this "reactive" scalar field is obtained from Eq. (5) without difficulty. In a Lagrangian framework we have

$$\frac{d}{dt}\Theta = F(\Theta), \tag{A.1}$$

where the forcing term

$$F(\Theta) = -\kappa(\langle\Theta\rangle_x - \beta y - \bar{\theta}), \tag{A.2}$$

accounts for the reactive dynamics. The above equation for Θ can be integrated along Lagrangian trajectories $\mathbf{x}_p(t)$. These are the solutions of Eq. (4) for the position of the virtual particles used in the reconstructions. Within this approach, the formal solution at time $t_2 > t_1$ is

$$\Theta(\mathbf{x}_p(t_2), t_2) = \Theta(\mathbf{x}_p(t_1), t_1) + \int_{t_1}^{t_2} F(\Theta(\mathbf{x}_p(s), s))\, ds. \tag{A.3}$$

Denoting $\Delta t = t_2 - t_1$, we have, for small Δt:

$$\Theta(\mathbf{x}_p(t_2), t_2) = \Theta(\mathbf{x}_p(t_1), t_1) + F(\Theta(\mathbf{x}_p(t_1), t_1))\Delta t. \tag{A.4}$$

The above equation can be used to modify our method of reconstruction. If all quantities at time t_1 (on the right hand side) are known at low resolution, the values at the particle positions can be computed by spatial interpolation to obtain the field Θ at higher resolution at a later time t_2 (on the left hand side). Iteration over longer time intervals is straightforward. Finally, notice that in the absence of forcing ($F = 0$) the purely advective reconstruction algorithm (Section 2) is recovered.

References

Abel, M., Celani, A., Vergni, D., Vulpiani, A., 2001. Front propagation in laminar flows. Phys. Rev. E 64, 046307.
Bartello, P., 2000. Using low-resolution winds to deduce fine structures in tracer. Atmos. Ocean 38, 303–320.
Batchelor, G.K., 1959. Small-scale variation of convected quantities like temperature in turbulent fluid. Part 1. General discussion and the case of small conductivity. J. Fluid Mech. 5, 113–133.
Bennett, A., 2006. Lagrangian Fluid Dynamics. Cambridge University Press (p. 286).
Berti, S., Dos Santos, F., Lacorata, G., Vulpiani, A., 2011. Lagrangian drifter dispersion in the southwestern Atlantic Ocean. J. Phys. Oceanogr. 41, 1659–1672.
Capet, X., McWilliams, J.C., Molemaker, M.J., Shchepetkin, A.F., 2008. Mesoscale to submesoscale transition in the California current system. Part I: flow structure, eddy flux, and observational tests. J. Phys. Oceanogr. 38, 29–43.
Cole, T.T., Rudnick, D.L., 2012. The spatial distribution and annual cycle of upper ocean thermohaline structure. J. Geophys. Res. 117, C02027.
Crisanti, A., Falcioni, M., Paladin, G., Vulpiani, A., 1991. Lagrangian chaos: transport, mixing and diffusion in fluids. Riv. Nuovo Cimento 14 (12), 1–80.
Desprès, A., Reverdin, G., d'Ovidio, F., 2011a. Mechanisms and spatial variability of mesoscale frontogenesis in the northwestern subpolar gyre. Ocean Model. 39, 97–113.
Desprès, A., Reverdin, G., d'Ovidio, F., 2011b. Summertime modification of surface fronts in the North Atlantic subpolar gyre. J. Geophys. Res. 116, 1–13.
Ferrari, R., 2011. A frontal challenge for climate models. Science 332, 316–317.
Hakim, G.J., Snyder, C., Muraki, D.J., 2002. A new surface model for cyclone-anticyclone asymmetry. J. Atmos. Sci. 59, 2405–2420.
Held, I., Pierrehumbert, R.T., Garner, S.T., Swanson, K.L., 1995. Surface quasi-geostrophic dynamics. J. Fluid Mech. 282, 1–20.
Isern-Fontanet, J., Chapron, B., Lapeyre, G., Klein, P., 2006. Potential use of microwave sea surface temperature for the estimation of ocean currents. Geophys. Res. Lett. 33 (L24608), 1–5.
Isern-Fontanet, J., Lapeyre, G., Klein, P., Chapron, B., Hecht, M.H., 2008. Three-dimensional reconstruction of oceanic mesoscale currents from surface information. J. Geophys. Res. 113 (C09005), 1–17.
Juckes, M., 1995. Instability of surface and upper-tropospheric shear lines. J. Atmos. Sci. 52, 3247–3262.
Keating, S.R., Smith, K.S., Kramer, P.R., 2011. Diagnosing lateral mixing in the upper ocean with virtual tracers: spatial and temporal resolution dependence. J. Phys. Oceanogr. 41, 1512–1534.
Klein, P., Lapeyre, G., 2009. The oceanic vertical pump induced by mesoscale and submesoscale turbulence. Annu. Rev. Mar. Sci. 1, 351–375.
Klein, P., Hua, B.L., Lapeyre, G., Capet, X., Le Gentil, S., Sasaki, H., 2008. Upper ocean turbulence from high-resolution 3D simulations. J. Phys. Oceanogr. 38, 1748–1763.
Koszalka, I., LaCasce, J.H., Ovik, K.A., 2009. Relative dispersion in the nordic seas. J. Mar. Res. 67, 411–433.
LaCasce, J.H., 1996. Baroclinic Vortices Over a Sloping Bottom (Ph.D. thesis). MIT/WHOI Joint Program in Physical Oceanography, p. 216.
LaCasce, J.H., 1998. A geostrophic vortex on a slope. J. Phys. Oceanogr. 28, 2362–2381.
LaCasce, J.H., Mahadevan, A., 2006. Estimating subsurface horizontal and vertical velocities from sea-surface temperature. J. Mar. Res. 64, 695–721.
LaCasce, J.H., Ohlmann, C., 2003. Relative dispersion at the surface of the Gulf of Mexico. J. Mar. Res. 61, 285–312.
Lapeyre, G., 2002. Characterization of finite-time Lyapunov exponents and vectors in two-dimensional turbulence. Chaos 12, 688–698.
Lapeyre, G., Klein, P., 2006. Dynamics of upper ocean layers in terms of surface quasigeostrophy theory. J. Phys. Oceanogr. 36, 165–176.
Ledwell, J.R., Watson, A.J., Law, C.S., 1993. Evidence for slow mixing across the pycnocline from an open-ocean tracer-release experiment. Nature 364, 701–703.

Legras, B., Pisso, I., Berthet, G., Lefèvre, F., 2005. Variability of the Lagrangian turbulent diffusion in the lower stratosphere. Atmos. Chem. Phys. 5, 1605–1622.

Le Traon, P.Y., Nadal, F., Ducet, N., 1998. An improved mapping method of multisatellite altimeter data. J. Atmos. Oceanic Technol. 15, 522–534.

Lévy, M., 2008. The modulation of biological production by oceanic mesoscale turbulence. Lect. Notes Phys. 744, 219–261.

Lévy, M., Klein, P., Tréguier, A.-M., 2001. Impact of sub-mesoscale physics on production and subduction of phytoplankton in an oligotrophic regime. J. Mar. Res. 59, 535–565.

Lumpkin, R., Elipot, S., 2010. Surface drifter pair spreading in the North Atlantic. J. Geophys. Res. 115, C12017.

Mariotti, A., Moustaoui, M., Legras, B., Teitelbaum, H., 1997. Comparison between vertical ozone soundings and reconstructed potential vorticity maps by contour advection with surgery. J. Geophys. Res. 102, 6131–6142.

Methven, J., Hoskins, B.J., 1999. The advection of high-resolution tracers by low-resolution winds. J. Atmos. Sci. 56, 3262–3285.

Orsolini, Y.J., Hansen, G., Manney, G.L., Livesey, N., Hoppe, U.P., 2001. Lagrangian reconstruction of ozone column and profile at the Lidar Observatory for Middle Atmosphere Research (ALOMAR) throughout the winter and spring 1997–1998. J. Geophys. Res. 106, 10011–10021.

Ottino, J.M., 1989. The Kinematics of Mixing: Stretching, Chaos and Transport. Cambridge University Press (p. 364).

Pascual, A., Faguère, Y., Larnicol, G., Le Traon, P.Y., 2006. Improved description of the ocean mesoscale variability by combining four satellite altimeters. Geophys. Res. Lett. 33 (L02611), 13–16.

Scott, R.K., 2006. Local and nonlocal advection of a passive scalar. Phys. Fluids 56, 122–125.

Shcherbina, A.Y., Gregg, M.C., Alford, M.H., Harcourt, R.R., 2010. Three-dimensional structure and temporal evolution of submesoscale thermohaline intrusions in the North Pacific subtropical frontal zone. J. Phys. Oceanogr. 40, 1669–1689.

Smith, K.S., Bocaletti, G., Henning, C.C., Marinov, I.N., Tam, C.Y., Held, I.M., Vallis, G.K., 2001. Turbulent diffusion in the geostrophic inverse cascade. J. Fluid Mech. 469, 14–47.

Sutton, R.T., Maclean, H., Swinbank, R., O'Neill, A., Taylor, F.W., 1994. High-resolution stratospheric tracer field estimated from satellite observations using Lagrangian trajectory calculations. J. Atmos. Sci. 51, 2995–3005.

Thomas, L.N., Lee, C.M., Yoshikawa, Y., 2010. The subpolar front of the Japan/East Sea. Part II: inverse method for determining the frontal vertical circulation. J. Phys. Oceanogr. 40, 3–25.

Tulloch, R., Smith, K.S., 2009. Quasigeostrophic turbulence with explicit surface dynamics: application to the atmospheric energy spectrum. J. Atmos. Sci. 66, 450–467.

Wang, J., Flierl, G.R., LaCasce, J.H., McClean, J.L., Mahadevan, A., 2013. Reconstructing the ocean's interior from surface data. J. Phys. Oceanogr. 43, 1611–1626.

Waugh, D.W., Abraham, E.R., 2008. Reconstructing the ocean's interior from surface data. Geophys. Res. Lett. 35 (L20605), 1–5.

Welander, P., 1955. Studies of the general development of motion in a two-dimensional, ideal fluid. Tellus 7, 141–156.